Interaction of Twin Synthetic Jets in Attached and Separated Boundary Layers - Effects of Yaw Angle and Phase Difference

XIN WEN [1*], HUI TANG[2], YINGZHENG LIU[1]

[1] Gas Turbine Research Institute, Shanghai Jiao Tong University

800 Dongchuan Road, Shanghai 200240, China

[2] Department of Mechanical Engineering, The Hong Kong Polytechnic University,

Kowloon, Hong Kong SAR, China

Submitted in May 2018

[*] Corresponding author.

E-mail address: wenxin84@sjtu.edu.cn (Xin WEN)

ABSTRACT

This paper further extends our understanding of the interaction between twin synthetic jets (SJs) in attached and separated laminar boundary layers, following our previous works on twin SJs at zero yaw angle [*J. Fluids Eng. - Trans. ASME* 139, 091203, et al.]. In current investigation, the twin-SJ induced streamwise vortices and their influence on attached and separated laminar boundary layers are examined at two non-zero yaw angles and four phase differences. Dye visualization and CFD simulations are conducted to compare the interaction of SJ-induced three-dimensional streamwise vortices and their impacts on the attached boundary layer. Two-dimensional PIV measurements are then conducted to evaluate the control effect of the twin SJs on the separated boundary layer. Our previous works have revealed that at zero yaw angle, the twin SJs interact in a constructive way regardless of their phase difference. Here we further find that, when the twin SJs operate with non-zero yaw angles, their interaction can be destructive due to the non-zero lateral distance, but the level of destruction can be mitigated by adjusting their phase difference. The strength of twin-SJ induced vortices and their impacts in the near-wall region are evaluated through streamwise vorticity flux and excess wall shear stress, respectively. In the separated boundary layer, although generally decreasing with the increase of yaw angle, significant influence of twin SJs can still be observed by varying the phase difference.

1. Introduction

Synthetic jet (SJ), also known as a zero-net-mass-flux jet, has been demonstrated as a promising method for active flow control (Glezer 1988; Amitay & Glezer 2002; Dandois et al. 2007; Tang et al. 2014; Salunkhe et al. 2016). Interactions of a circular SJ and a crossflow can induce groups of streamwise vortices and effectively energize the boundary layer flow (Ramasamy et al. 2010). Among the different vortices, hairpin vortices were found to delay flow separation in boundary layers (Zhang & Zhong 2010; Zhong & Zhang 2013). In order to expand the influenced area, SJ arrays instead of single SJs are more commonly implemented. Therefore, it is critical to understand the interaction of the multiple streamwise vortices under different SJ-array configurations and evaluate their control effects. As one of the important parameters of the array configuration, phase difference was focused in our previous investigations on in-line twin SJs (Wen et al., 2015; Wen and Tang, 2016; Wen et al. 2016; Wen and Tang, 2017). Three types of streamwise vortices were identified in attached boundary layers: one combined vortex at phase difference $\Delta\phi = \pi/2$, two completely separated vortices at $\Delta\phi = 3\pi/2$, and partially interacting vortex structures at $\Delta\phi = 0$ and π. In separated boundary layers, these vortices also provided distinct flow control effects.

However, only very limited studies were reported on another important parameter: the yaw angle ψ, i.e., the angle between the line connecting the orifice centers of the twin SJs and the boundary layer flow direction. For example, the twin SJs may yield a larger influenced area under a larger yaw angle. However, the three-dimensional nature of the SJ-induced streamwise vortices makes it challenging to examine the interaction between them. From observations of surface flow visualization, Watson et al. (2003) hypothesized that the twin SJs would interact constructively with $\psi = 0$ (or in-line arrangement), resulting in a single stronger streamwise vortex. At yaw angle $\psi = \pi/12$, they found that the inner vortex tubes of both SJs interacted destructively since the tubes rotated in opposite direction, leaving only two outer tubes. From time-averaged flow fields obtained by PIV measurement, Liddle et al (2005) confirmed twin SJs can interact in a constructive manner with $\psi = 0$, but did not find the destructive interaction at $\psi = \pi/12$. In real world applications, the yaw angle and the phase difference of SJ arrays are usually both taken into account to find the optimal configuration. Accordingly, it is highly desirable to examine the interactions of the twin SJs under different array configurations and evaluate their flow control effects.

In the present study, we investigate the influence of the *yaw angle* and *phase difference* on the interaction of twin SJs in an attached/separated laminar boundary layer. To best visualize the flow structures and analyze the interactions, both experimental and numerical methodologies are used. In the attached boundary layer, stereo color dye visualizations in a water tunnel and CFD simulations are conducted to examine the induced three-dimensional vortex structures and their impacts on the attached boundary layer. The strength of the vortices is evaluated using streamwise vorticity flux. To assess the influence of the flow structures on the boundary layer in the near-wall region, excess wall shear stress is also calculated and compared. In the separated boundary layer, PIV measurements are implemented in the water tunnel to evaluate the performance of the induced streamwise vortices on flow separation control.

2 Methodology

2.1 Experimental platform

The experimental platform used in this study is similar to that used in our previous studies (Wen et al. 2015, Wen & Tang 2016, Wen et al. 2016; Wen and Tang, 2017). The same low-speed water tunnel with a test section of 1 m (L) × 0.45 m (W) × 0.45 m (H) is used. Figure 1a shows a sketch of the test plate and its coordinate system. The boundary layer develops along the horizontal Plate 1, and will firstly separate at some point on transitional Plate 2 or inclined Plate 3, generating a separated region. Two SJ actuators are mounted on Plate 1, with their orifices flush to the lower surface. As shown in the close-up view in Fig. 1b, each SJ actuator has a cylindrical cavity with an oscillating diaphragm clamped to its top side. The diaphragms are driven by two permanent magnetic shakers in a piston-like sinusoidal manner. The two orifices have the same diameter D_o = 5 mm and their center-to-center distance is fixed at d = 10 mm, i.e., d/D_o = 2. Further description of the experimental platform can be found in our previous works (Wen et al. 2015, Wen & Tang 2016, Wen et al. 2016). For current test rig, the twin SJ actuators can be rotated together accordingly to the midpoint point of the two orifices, resulting in the changing of the yaw angle ψ from 0 to $\pi/2$. Here, 0 indicates the in-line configuration and $\pi/2$ the perpendicular configuration. The origin of the coordinate system is set at the midpoint of the two orifices, with x axis pointing to the crossflow flow direction, y axis downward, and z axis to the spanwise direction.

2.2 Case selection

Current case is selected to ensure that hairpin vortices are induced, which has same working conditions to our previous studies (Wen et al. 2015, Wen & Tang 2016, Wen et al. 2016). Under these conditions, the dimensionless stroke length has a value of L = 1.7, which indicates the length of jet column in one period non-dimensionalized by the orifice diameter. The velocity ratio is VR = 0.16, which is the ratio of the SJ velocity to the freestream velocity. To yield the above values, the freestream velocity has a crossflow velocity of U_∞ = 0.11 m/s. The diaphragms of the SJ actuators have a peak-to-peak displacement of Δ = 0.105 mm and a frequency of f = 2 Hz. The interaction of the twin SJs is then examined at two selected yaw angles, i.e. $\psi = \pi/4$ and $\pi/2$, with the twin actuators operating with four different phase differences, i.e. $\Delta\phi = 0$, $\pi/2$, π, and $3\pi/2$. Here the phase difference $\Delta\phi$ is defined as the phase lag of the downstream actuator to the upstream one. To define the actuation period, diaphragm movement of the

upstream actuator is used: t/T = 0 (and 1), 1/4, 1/2, and 3/4 correspond to the beginning of blowing, maximum blowing, beginning of ingestion, and maximum ingestion, respectively, where T is the actuator operation period.

2.3 Stereoscopic color dye visualization system

Food dye with two distinct colors is used to better visualize and differentiate the twin SJs in the crossflow. As shown in Fig. 1a, red dye is filled in the upstream SJ actuator and green dye for the downstream one. Methanol is mixed into the dye to achieve a density very close to the water's. The flow patterns of the induced streamwise vortices are captured simultaneously from side view and bottom view by a color high-speed camera and a digital single-lens reflex (DSLR) camera, respectively. Details of the dye visualization setup can be found in our previous works (Wen et al. 2015; Wen & Tang 2016).

2.4 Particle image velocimetry (PIV)

To evaluate effects of the twin SJs on flow separation control, PIV measurements are conducted in a plane parallel to the inclined Plate 3 in the separated flow. Inside the water tunnel, Dantec polyamide seeding particles of 20 μm diameter are used to track the water flow. A 200 mJ double pulsed Nd:YAG Laser fires a light sheet of approximately 2 mm thickness to illuminate the seeding particles. To keep the light reflection at an acceptable level, a distance of about 5 mm, i.e. $1D_o$, is used between the light sheet and the inclined Plate 3. Inside the illuminated area, a field of view of $x = 35D_o \sim 57D_o$ and $z = -13D_o \sim 13D_o$ is captured by high speed camera to cover both the forward and backward flow portions of the separated flows. To resolve the corresponding vectors, a two-frame algorithm is used to cross correlate a 32×32 pixel interrogation area with an overlap ratio of 50%. This gives a 1.5mm spatial separation between adjacent vectors. The overall relative error of the measured velocity components is about 1% (Wen et al. 2015). To obtain time averaged flow fields, 200 pairs of PIV images are used.

2.5 Numerical approach

CFD simulations are applied to obtain details of the three-dimensional streamwise vortices and their impacts on the attached boundary layer. The boundary conditions and numerical settings are identical to those used in our previous work (Wen & Tang 2014). Therefore, they are only briefly introduced here. At the boundaries of the actuator diaphragms, a time-dependent velocity boundary condition is utilized at the

diaphragm's neutral position, described as

$$u_d(t) = \pi \Delta f \sin(2\pi f t) \quad (1)$$

At the crossflow inlet boundary, a Blasius velocity profile is applied to ensure a laminar boundary layer. The total mesh number of about 3 million is used in the simulations. A commercial CFD code, ANSYS FLUENT 13.0, is utilized to solve the unsteady, three-dimensional incompressible Navier–Stokes equations. The second-order implicit scheme and the second-order upwind scheme are used to discretize the equations in time and in space, respectively. For pressure–velocity coupling, the Pressure-Implicit with Splitting of Operators (PISO) method is applied. The time step size is set as 1/120 of the diaphragm oscillation cycle as a compromise between computational accuracy and time. This simulation framework has been well validated by comparing with our PIV results (Wen 2015). The working conditions in the simulation are set the same as those in the experiment.

To identify the SJ-induced vortex structures, a widely used Q criterion is applied on the three dimensional flow fields (Hunt *et al*. 1988). The quantity Q is defined as $Q = (||X||^2 - ||S||^2)/2$, where S and X are the symmetric and anti-symmetric components of velocity gradient, respectively, and $||\cdot||$ represents the norm of a given tensor. The Q-criterion proposes that an iso-surface of a positive Q value defines a vortex structure. In current study, a Q value of 30 is selected to let the major vortex structures stand out.

2.6 Streamwise vorticity flux

To examine strength of the SJ-induced streamwise vortices in the attached boundary layer, vorticity flux J_x along streamwise direction is used (Chang et al. 2009; Song et al. 2016). Here, J_x is calculated in a selected spanwise wall-normal plane at $x = 6D_o$ in the flow fields obtained from CFD simulations. The streamwise vorticity is integrated along wall-normal (y) direction to examine the spanwise (z) distribution of J_x, as

$$J_x = \frac{\Delta z}{A} \int_{y=0}^{y=\delta} |\omega_x| \, dy \tag{2}$$

where A is the total integrating area, Δz the width of integrating area in spanwise direction, δ the thickness of the boundary layer in wall-normal direction and $|\omega_x|$ the absolute value of the streamwise vorticity.

3 Results and discussion

3.1 Interaction in the attached boundary layer

The interaction of hairpin vortices issued from the twin SJs at two non-zero yaw angles, i.e., $\psi = \pi/4$ and $\pi/2$, are focused here.

3.1.1 At yaw angle $\psi = \pi/4$

Fig. 2 presents the flow patterns captured by the dye visualizations at $\psi = \pi/4$. At phase difference $\Delta\phi = \pi/2$, the two SJ-induced hairpin vortices form and propagate downstream side by side, hence their inner legs interact with each other (Fig. 2b). These two inner legs rotate in opposite directions and hence tend to cancel out each other, interacting in a destructive manner. By changing the phase difference to $\Delta\phi = 3\pi/2$, the hairpin vortices issued from the two actuators are almost evenly distributed in the streamwise direction, resulting in a doubled occurrence rate for hairpin vortices (see Fig. 2d). This far distance also mitigates the destructive interaction. Hence the coherence of the hairpin vortices can be better maintained. In addition, a clear snake creeping locomotion shape is observed from the bottom view. It is caused by the attraction of each hairpin vortex's inner leg tail towards the mid-span plane that is exerted by the in-wash flow induced around its neighboring hairpin head. At $\Delta\phi = 0$ and π, intermediate interactions of the hairpin vortices are shown in Figs. 2a and 2c, respectively. It is observed that the vortices in the $\Delta\phi = \pi$ (anti-phase) case are more capable of maintaining their coherence than those in the $\Delta\phi = 0$ (in-phase) case. In the latter case, the trailing hairpin vortex is obviously attracted towards the mid-span plane.

From CFD simulations, the induced three-dimensional vortex structures are captured by the iso-surface of $Q = 30$ with contours of streamwise vorticty, as shown in Figs. 3 and 4. These results not only confirm the observations in dye visualization, but also reveal some new findings. A sequence of snapshots is presented in Fig. 3 to examine the evolution of the twin SJs at $\Delta\phi = 0$. It is confirmed that the trailing hairpin vortex is attracted towards the mid-span plane. In addition, the downstream actuator can exert an important influence on the trailing hairpin vortex. At the early stage of the oscillation period, the two hairpin vortices travel almost independently after emerging from the actuators until when the twin actuators start ingestion ($t/T = 0.5$). At the maximum and end of ingestion ($t/T = 0.75$ and 1), the trailing hairpin vortex is attracted towards the mid-span plane. This is caused by the downstream actuator which

induces a strong ingestion flow when the trailing hairpin vortex passes by. In addition, the inner leg of the trailing hairpin vortex gains strength from the ingestion flow, whereas the outer leg is weakened. This leads to an obvious difference between the two legs as shown in Fig. 3a. It also provides explanation for the interaction between the inner legs at $\Delta\phi = \pi/2$. As shown in Fig. 4a, the inner leg of hairpin vortex issued from the downstream actuator is very weak due to the destruction interaction. However, the inner leg of its counterpart issued from the upstream actuator is obviously stronger. This is because it gains strength from the ingestion flow induced by the downstream actuator. At $\Delta\phi = \pi$ and $3\pi/2$, the influence of the downstream actuator is not significant as observed in Figs. 4b and 4c. At $\Delta\phi = 3\pi/2$, the inner legs are stronger than the outer ones, because these counter-rotating vortices are no longer forced to collide due to their increased streamwise spacing. Under such configuration, they are arranged in line with the streamwise direction. The head of the trailing inner leg laps over the tail of the leading one, strengthening each other.

The induced streamwise vortices also have very different strength. To examine the variation of their strength, plots of the time-averaged streamwise vorticity flux J_x in the spanwise wall-normal plane at $x = 6D_o$ are presented in Fig. 5. The values of J_x are calculated from CFD simulations, and the plot of single SJ case is added as a reference. For the single SJ case, the J_x profile has two peaks that are separated by the center line. The two peaks are caused by the two hairpin legs. The variation trend of the J_x for the twin SJs reflects their interactions. At $\Delta\phi = \pi/2$, the profile has lowest peaks among all five cases, indicating the destructive interaction. The reduction in J_x is most significant around $z = -0.4D_o$ due to weakened inner leg of the hairpin vortex issued from downstream actuator. On the other hand, at $\Delta\phi = 3\pi/2$, the J_{ABS} profile has the highest peak value, more than 1.5 times of that in the single SJ case, indicating the constructive interaction between the inner legs. It has only one peak, since strengthened inner legs propagate in line along the mid-span plane. At $\Delta\phi = 0$ and π, the J_x profiles are generally similar but symmetrical to each other about the center line. They have one peak higher than that of single SJ case, but one peak lower on the other side of the center line. Thus, these profiles indicate an intermediate interaction between the two hairpin vortices.

To further assess the capability of the streamwise vortices in influencing the boundary layer, the excess wall shear stress due to the passage of twin-SJ induced flow structures at various phase differences is calculated and compared. Here the excess wall shear stress is defined as $(\tau_w - \tau_{w,nojet})/\tau_{w,nojet}$, the

normalized difference in wall shear stress between with and without the SJs. Fig. 6 compares the spanwise distribution of the time-averaged excess wall shear stress at two selected locations, i.e., $x = 6D_o$ and $18D_o$. At $x = 6D_o$ that is near the downstream orifice, the profile has two peaks that are separated by a trough in the single SJ case, which has a similar shape of the J_x profile (Fig. 5). For the twin SJ cases, the variation trend of the wall shear stress profiles is generally in consistence with the J_x strength. The twin hairpin vortices at $\Delta\phi = 3\pi/2$ exert strongest impact in the near wall region, whereas they exert weak influence at $\Delta\phi = \pi/2$. At $x = 18D_o$ that is far from the two orifices, unexpected high wall shear stress is observed at $\Delta\phi = \pi/2$. To examine the reason, corresponding time-averaged flow field is plotted on the spanwise-wall-normal plane at $x = 18D_o$. As shown in Fig. 7, there is a strong downwash flow induced between the inner legs of the two hairpin vortices. This downwash flow can bring outer high-momentum fluid to the near wall region, and energize the near wall flow.

3.1.2 At yaw angle $\psi = \pi/2$

At yaw angle $\psi = \pi/2$, the two SJ actuators are arranged perpendicular to the boundary layer flow direction. As such, compared to that in the other yaw angle cases, the lateral distance of these two actuators is the largest. Fig. 8 presents the flow patterns captured by dye visualizations. In general, the interaction of the twin SJs is similar to that at $\psi = \pi/4$. However, the preferable phase difference, which maximizes the streamwise spacing and minimizes the destructive interaction between the two hairpin vortices, shifts to $\Delta\phi = \pi$ as shown in Fig. 8c. The reason is that the zero streamwise orifice distance at $\psi = \pi/2$ causes an even distribution of hairpin vortices issued from the two actuators at $\Delta\phi = \pi$. The simulated vortex structures are also presented in Fig. 9. Since the flow structures at phase differences $\Delta\phi = \pi/2$ and $3\pi/2$ are almost mirrored to each other as demonstrated in the dye visualization, the CFD results are presented only for the first three phase differences, i.e. $\Delta\phi = 0$, $\pi/2$ and π. Fig. 9a confirms that the inner legs of the twin hairpin vortices are weakened at $\Delta\phi = 0$, which is indicated by the slim shapes. In addition, the inner legs are pushed away from mid-span plane, leaving a large gap between them. In Fig. 10, the spanwise-wall-normal plane $x = 6D_o$ (as indicated in Fig. 9a) is selected to examine the repelling interaction. It shows that there is a stagnation flow region formed between the inner legs. This stagnation flow region is generated by downwash flow induced by the inner legs and the increased lateral distance between the two actuators. Since this stagnation flow region is constrained by the wall, the accumulated fluid will push the

inner legs outboard. The simulated flow structures at $\Delta\phi = \pi/2$ and π are quite similar to those captured by dye visualizations.

The strength of the induced streamwise vortices by twin SJs at $\psi = \pi/2$ is examined by time-averaged streamwise vorticity flux J_x as shown in Fig. 11. In consistence with the interaction manners observed from the flow structures, the profile has lowest peaks at $\Delta\phi = 0$. Due to the stagnation flow region, J_{ABS} has much lower values around the centerline, even lower than that in the single SJ case. At $\Delta\phi = \pi$, the profile has two highest peaks, which are close to the centerline. At $\Delta\phi = \pi/2$, the profile shows an intermediate level.

Fig. 12 presents the spanwise distribution of the time-averaged excess wall shear stress. There is an obvious changing between the profiles at the two selected locations, i.e., $x = 6D_o$ and $18D_o$. At $x = 6D_o$, the variation trend of the excess wall shear stress is closely related to the induced flow structures. The profile of excess wall shear stress at $\Delta\phi = 0$ has two pairs of weak peaks symmetrical about the center line. On the other hand, profiles at $\Delta\phi = \pi/2$ and π have a single and much stronger peak at the center line. At $x = 18D_o$, due to the spreading of the flow structures, the inner peaks begin to merge at $\Delta\phi = 0$, resulting in an increase of the excess wall shear stress at the center line. At $\Delta\phi = \pi$, the peak at the center line spreads to outer sides and splits into one pair of lateral peaks. Similarly, at $\Delta\phi = \pi/2$ the peak at center line also becomes weaker due to the penetration of the flow structures in the boundary layer.

3.2 Interaction in the separated boundary layer

To examine the flow control effects of the twin SJs with different alignments, the induced flow structures at yaw angles of $\psi = \pi/4$ and $\pi/2$ are applied to the same laminar boundary layer that is separated from the wall. In the wall-parallel measurement plane, Fig. 13 shows time-averaged streamwise velocity contours plus streamlines for the uncontrolled and single-SJ controlled cases. The mainstream flows from the bottom to the top in the plan-view figures. As shown in Fig. 13a, the mainstream separates from the wall along an almost straight spanwise line. The separation line is indicated either by the interface (the white region) between the forward flow (lower red region) and the reversed flow (upper blue region) or by the spanwise streamlines. To further evaluate the control effects, a quantity, S_L, is calculated to describe the mean streamwise location of the separation line. The value of S_L is obtained from an area with a spanwise range $z = -5D_o \sim 5D_o$, within which the most influence of the SJs is exerted. In the uncontrolled case, S_L has a streamwise location of $39.0D_o$. When a single SJ is applied, the forward flow shows a slight protrusion into the reversed flow in Fig. 13b, which spans about $4D_o$ and protrudes to $x = 43D_o$. The mean separation line is slightly delayed to $S_L = 40.9D_o$.

At yaw angle $\psi = \pi/4$, the twin SJs can induce stronger streaks of forward flow protrusions than the single SJs, regardless of the phase difference, as shown in Fig. 14. This is similar to our previous findings at yaw angle $\psi = 0$. However, the enhancement is limited due to the destructive interactions between the twin SJs. The mean streamwise locations of the separation lines at phase differences $\Delta\phi = 0$ and π for yaw angle $\psi = \pi/4$ are only delayed a little to $S_L = 42.1D_o$ and $43.5D_o$, respectively, as shown in Figs. 14a and 14c. At $\Delta\phi = \pi/2$ in Fig. 14b, the forward flow is obviously stronger along the mid-span plane. Due to the strong forward flow, a recirculation zone is induced on the right-hand side. The mean location of the separation line is much delayed to $S_L = 46.8D_o$. This is not surprising and is in consistence with the high excess wall shear stress induced by the strong downwash flow in the attached boundary layer (Figs. 6b and 7). As the phase difference increases to $\Delta\phi = 3\pi/2$, the forward-flow streak is strongest as shown in Fig. 14d. The forward flow spans about $5D_o$ and protrudes beyond the upper boundary of current measurement field, i.e., $x = 57D_o$. It is also accompanied by a pair of large recirculation zones on both sides. The mean location of the separation line is significantly delayed to $S_L = 49.5D_o$. As discussed above at $\Delta\phi = 3\pi/2$, the inner legs of the hairpin vortices are much stronger than the outer ones in the attached boundary layer. The flow structures exert flow control effect concentrated along the mid-span plane,

resulting in a slim forward-flow streak in the originally separated flow region. In addition, the twin hairpin vortices evenly distribute in streamwise direction with less interaction and doubled frequency. Therefore, they can exert intensive and lasting flow control.

At yaw angle $\psi = \pi/2$, compared with those at $\psi = \pi/4$, the flow control effects of the twin SJs are generally weaker, as shown in Fig. 15. At $\Delta\phi = 0$ as shown in Fig. 15a, the shape of the forward-flow streak is similar to that in the single SJ case, but is wider in the spanwise direction. This is because the twin hairpin vortices travel side by side, exerting a large region of influence. The streamwise location of mean separation line is $S_L = 41.5D_o$, slightly delayed compared with that induced by the single SJ. The forward-flow streak is strongest at $\Delta\phi = \pi$ as shown in Fig. 15c, which shares a similar shape to that at $\Delta\phi = 3\pi/2$ in the $\psi = \pi/4$ arrangement, but in a weaker manner. As discussed above, this is because the flow structures induced by the twin SJs are similar in these two cases. However, due to the increased spanwise distance at $\psi = \pi/2$, the interaction between the twin SJs is weaker. The streak has a narrow span of about $5D_o$ and protrudes deeply to $x = 56D_o$. The streamwise location of the mean separation line is also delayed remarkably to $S_L = 44.1D_o$. At $\Delta\phi = \pi/2$ and $3\pi/2$, the streaks show intermediate patterns with $S_L = 41.5D_o$ and $S_L = 42.3D_o$, respectively, as shown in Fig. 15b and 15d.

4 Conclusions

The interactions of twin SJs with an attached laminar boundary layer along a flat plate and with a separated laminar boundary layer flow over inclined plates are investigated using both experimental and numerical methods. The twin SJs are arranged with two non-zero yaw angles and operate with four phase differences. The main findings from this study are summarized as follows:

(i) In the attached boundary layer, the interaction between the twin SJs can be destructive, resulting in less coherent flow structures with weak streamwise vorticity flux as well as weak impact in the near wall region. At yaw angle $\psi = \pi/4$, the most destructive interaction happens at phase difference $\Delta\phi = \pi/2$, whereas it happens at $\Delta\phi = 0$ for $\psi = \pi/2$ because of the zero streamwise distance between the two SJ actuators. In both cases, the twin SJs travel side by side with close location in both streamwise and spanwise directions. The counter-rotating inner legs of the twin SJs tend to weaken each other, resulting in the destructive interaction. At $\psi = \pi/4$, the downstream actuator can also exert strong influence on the trailing hairpin vortex issued from upstream actuator at $\Delta\phi = 0$ and $\pi/2$.

(ii) The level of destructive interaction between the twin SJs can be mitigated by tuning their phase difference. At yaw angle $\psi = \pi/4$, as $\Delta\phi$ increases to $3\pi/2$, the destructive interaction is much mitigated. Due to the increase in the streamwise distance between them, the inner legs are strengthened during the interaction. Strong and concentrated streamwise vorticity flux and high excess wall shear stress are induced along the mid-span plane. At yaw angle $\psi = \pi/2$, the favorable phase difference is shifted to $\Delta\phi = \pi$, resulting in similar flow structures, but with weaker interaction.

(iii) The delay of flow separation is indicated by a streak of forward flow protrusion into the reversed flow. At yaw angle $\psi = \pi/4$, stronger streaks of forward flow protrusions are induced by the twin SJs than by a single SJ, regardless of the phase difference. Due to the constructive interaction and double occurrence frequency, the twin SJs exert strongest control effect at $\Delta\phi = 3\pi/2$. At yaw angle $\psi = \pi/2$, the flow control effects become weaker compared with those at $\psi = \pi/4$. In consistent with the behavior of the SJ-induced flow structures, the strongest forward flow is induced at $\Delta\phi = \pi$, which shares a similar slim shape to that at $\Delta\phi = 3\pi/2$ in $\psi = \pi/4$ arrangement.

This investigation furthered our understanding of the interaction of twin SJs in attached/separated laminar boundary layers, which would be useful for future SJ-array applications.

Acknowledgments

The first author of this paper, Dr. Xin Wen, would like to acknowledge the financial support from Nanyang Technological University for his PhD study. The authors gratefully acknowledge the financial support from the National Natural Science Foundation of China (Grant No. 11702172 and 11725209) for this study.

References

1. Amitay, M. and Glezer, A. Role of Actuation Frequency in Controlled Flow Reattachment over a Stalled Airfoil. AIAA Journal 2002 ;40(2):209-216.
2. Chang, L.M., Wang, L.B. and Song, K.W., Numerical study of the relationship between heat transfer enhancement and absolute vorticity flux along main flow direction in a channel formed by a flat tube bank fin with vortex generators. International Journal of Heat & Mass Transfer, 2009, 52(7–8):1794-1801.
3. Dandois, J., Garnier, E and Sagaut, P. Numerical simulation of active separation control by a synthetic jet. Journal of Fluid Mechanics 2007;574:25.
4. Glezer, A. The formation of vortex rings. Physics of Fluids 1988;31(12):3532-3542.
5. Hunt, J., Wray, A., and Moin, P., Eddies, streams, and convergence zones in turbulent flows. Proceedings of the 1988 Summer Program, Center For Turbulence Research, Stanford University, 1988, 193-208.
6. Liddle, S, Wood, N. Investigation into clustering of synthetic jet actuators for flow separation control application. The Aeronautical Journal 2005;35-44.
7. Ramasamy, M, Wilson, J.S., and Martin, P.B. Interaction of Synthetic Jet with Boundary Layer Using Microscopic Particle Image Velocimetry. Journal of Aircraft 2010;47(2):404-422.
8. Salunkhe, P., Tang, H., Zheng, Y., and Wu, Y., PIV measurement of mildly controlled flow over a straight-wing model, International Journal of Heat and Fluid Flow 2016; 62: 552-559.
9. Song, K.W, Liu, S. and Wang, L.B., Interaction of counter rotating longitudinal vortices and the effect on fluid flow and heat transfer, International Journal of Heat & Mass Transfer 2016, 93:349-360.
10. Tang, H., Salunkhe, P., Zheng, Y., Du, J., Wu, Y. On the use of synthetic jet actuator arrays for active flow separation control. Experimental Thermal and Fluid Science 2014;57:1-10.
11. Watson, M., Jaworski, A.J., and Wood N.J. Contribution to the understanding of flow interactions between multiple synthetic jets. AIAA Journal 2003;747-749.
12. Wen, X. Study of Synthetic Jets in Boundary layers. PhD thesis, Nanyang Technological University, Singapore, 2015.
13. Wen, X. and Tang, H. On hairpin vortices induced by circular synthetic jets in laminar and turbulent boundary layers. Computers & Fluids 2014;95(0):1-18.

14. Wen, X., Tang, H. and Duan, F., Vortex dynamics of in-line twin synthetic jets in a laminar boundary layer, Physics of Fluids 2015;27(8):083601.
15. Wen, X., and Tang, H., Effect of Phase Difference on the Interaction of Hairpin Vortices Induced by In-line Twin Synthetic Jets, Journal of Visualization, 2016;19(1), 79-87.
16. Wen, X., Tang, H., and Duan, F., Interaction of In-line Twin Synthetic Jets with a Separated Flow, Physics of Fluids, 2016, 28, 043602.
17. Wen, X. and Tang, H., Dye Visualization of In-line Twin Synthetic Jets in Crossflows - A Parametric Study, Journal of Fluids Engineering, 2017, 139(9), 091203
18. Zhang, S. and Zhong, S. Experimental Investigation of Flow Separation Control Using an Array of Synthetic Jets. AIAA Journal 2010;48(3):611-623.
19. Zhong, S. and Zhang, S. Further Examination of the Mechanism of Round Synthetic Jets in Delaying Turbulent Flow Separation. Flow, Turbulence and Combustion 2013;91(1):177-208.

Figure 1

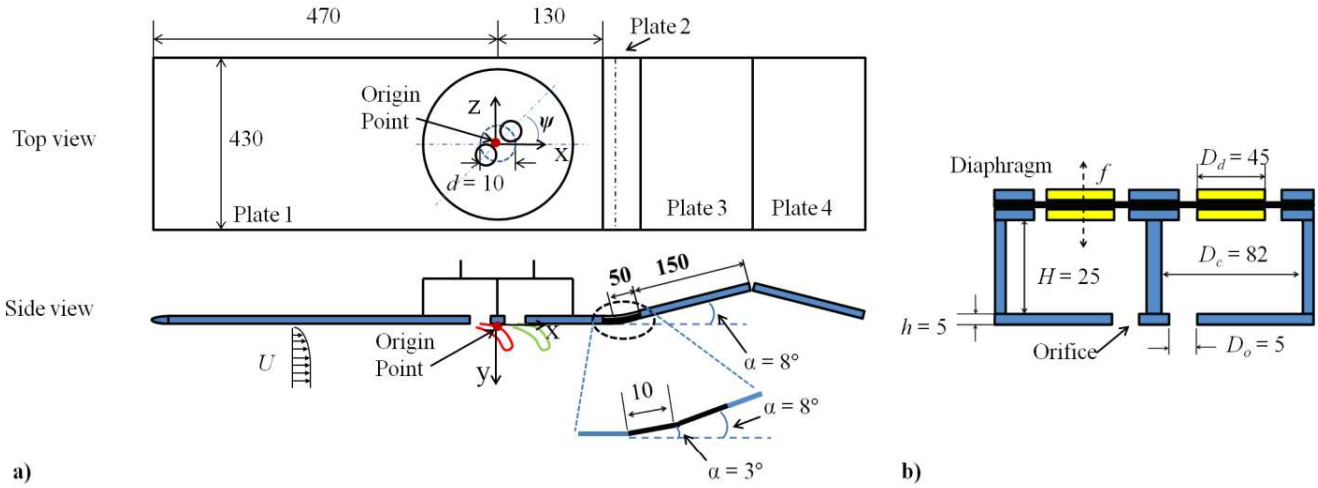

Schematic of (a) the test plate and (b) the SJ actuators (not to scale, all dimensions are in mm).

Figure 2

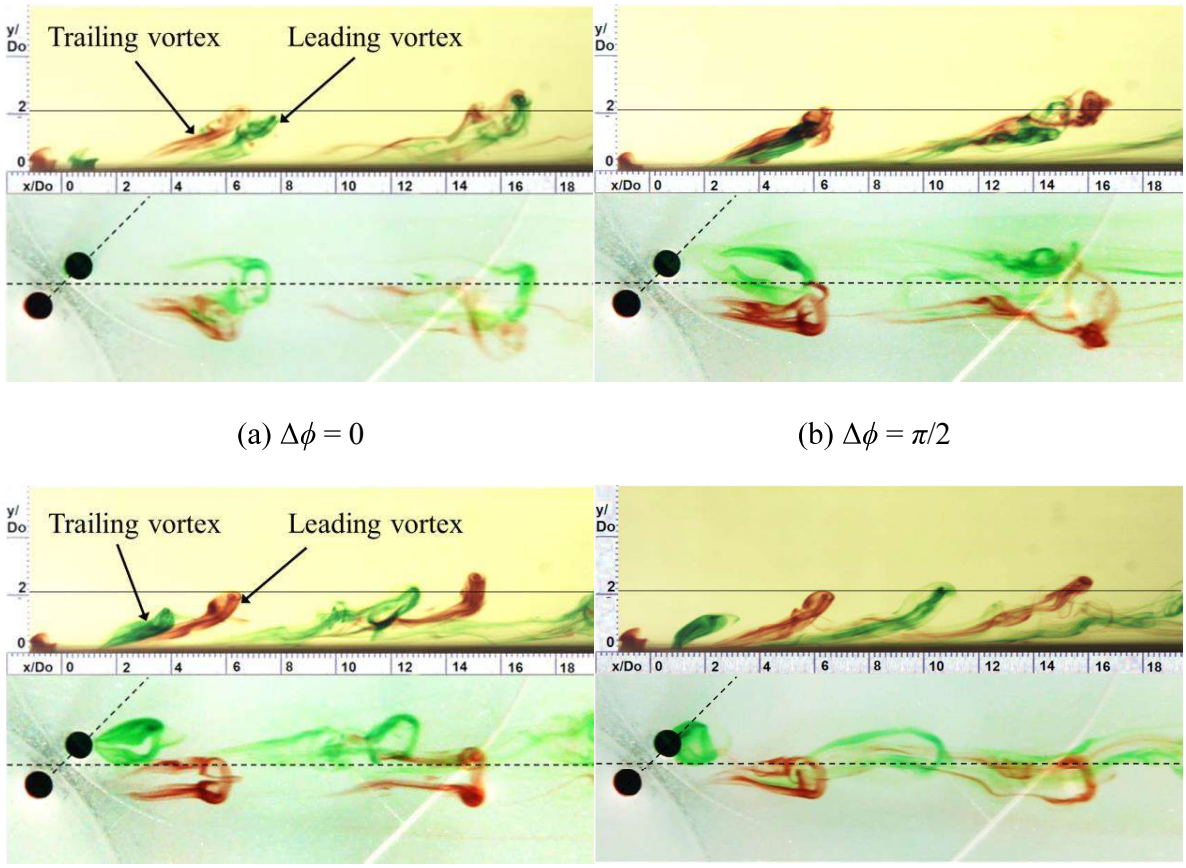

(a) $\Delta\phi = 0$ (b) $\Delta\phi = \pi/2$

(c) $\Delta\phi = \pi$ (d) $\Delta\phi = 3\pi/2$

Stereoscopic dye visualizations of twin SJs at yaw angle $\psi = \pi/4$ with four phase differences $\Delta\phi$.

Figure 3

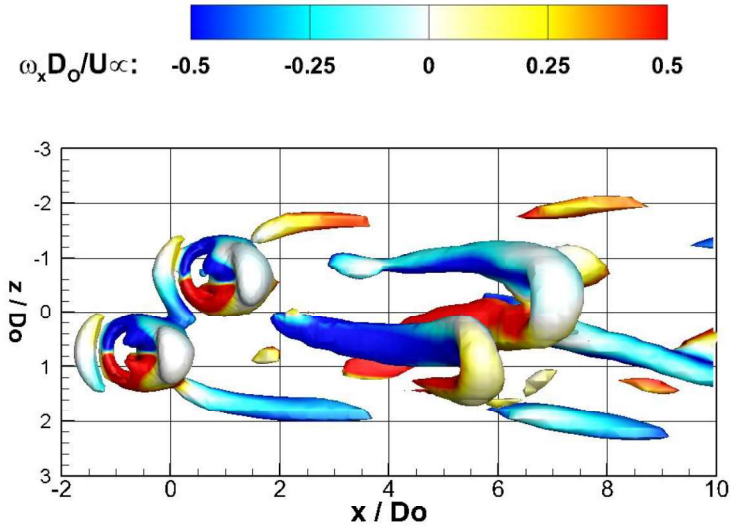

(a) t / T = 0.25

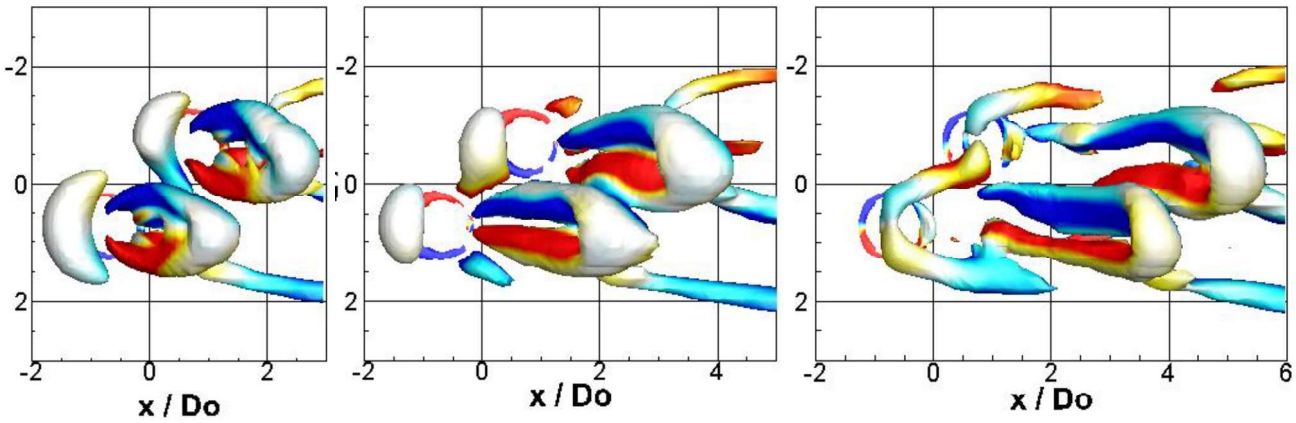

(b) t / T = 0.5 (c) t / T = 0.75 (d) t / T = 1.0

A sequence of snapshots of instantaneous flow structures from bottom view is plotted with $Q = 30$ from CFD simulations at phase difference $\Delta\phi = 0$ and yaw angle $\psi = \pi/4$. The contours represent streamwise vorticity.

Figure 4

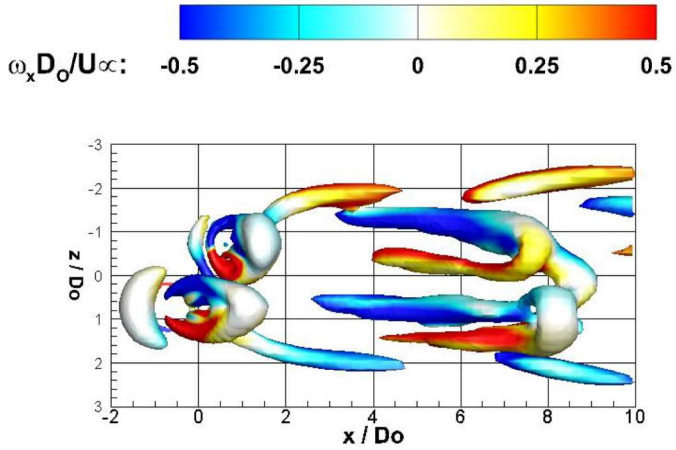

(a) $\Delta\phi = \pi/2$

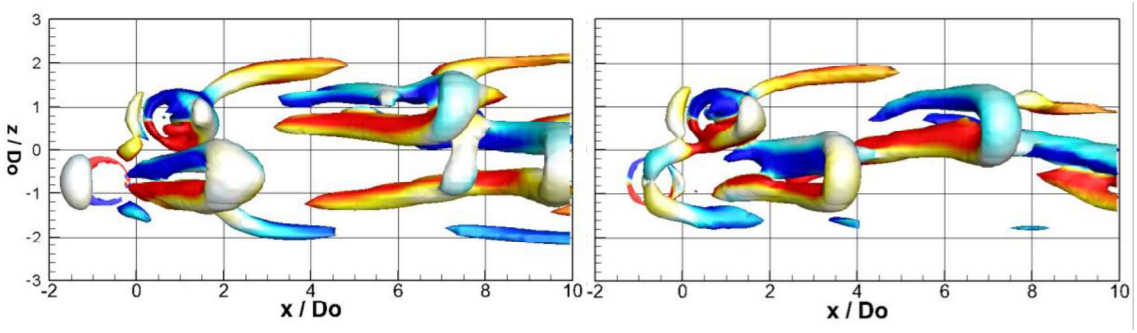

(b) $\Delta\phi = \pi$ (c) $\Delta\phi = 3\pi/2$

Bottom views of instantaneous flow structures plotted with $Q = 30$ from CFD simulations at yaw angle $\psi = \pi/4$ with three non-zero phase differences $\Delta\phi$.

Figure 5

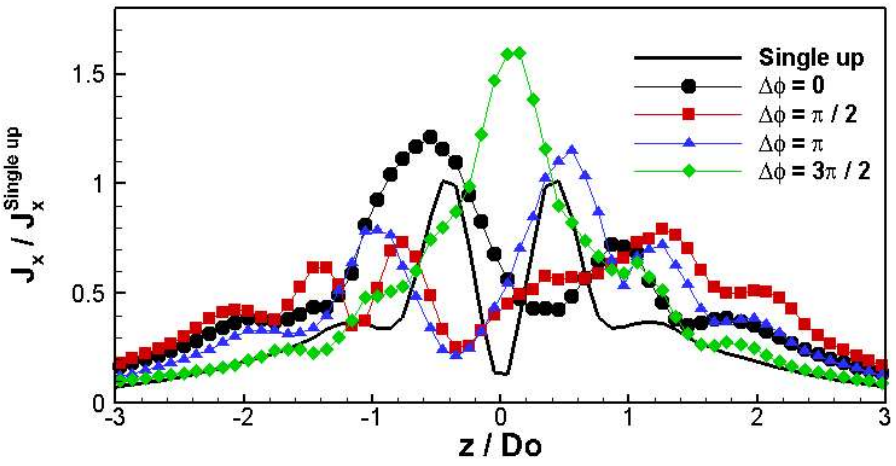

Spanwise distribution of time-averaged streamwise vorticity flux in a wall-normal plane at $x = 6D_o$ in single SJ case and twin SJ cases at yaw angle $\psi = \pi/4$ with four phase differences $\Delta\phi$. The absolute vorticity flux is normalized by the peak value of that in single SJ case.

Figure 6

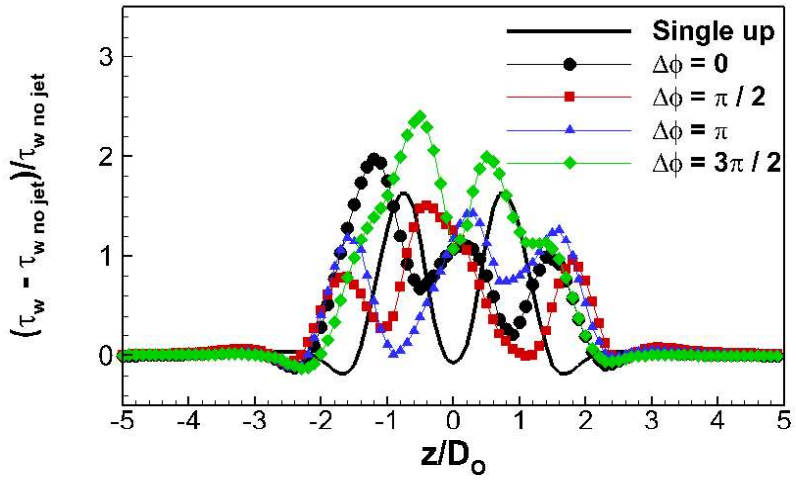

(a)

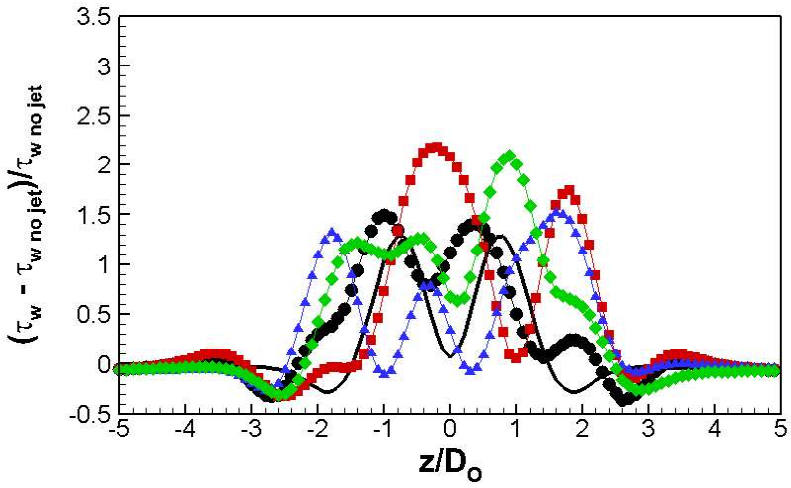

(b)

Spanwise distribution of time-averaged excess wall shear stress at (a) $x = 6D_o$ and (b) $x = 18D_o$ at yaw angle $\psi = \pi/4$ with four phase differences $\Delta\phi$.

Figure 7

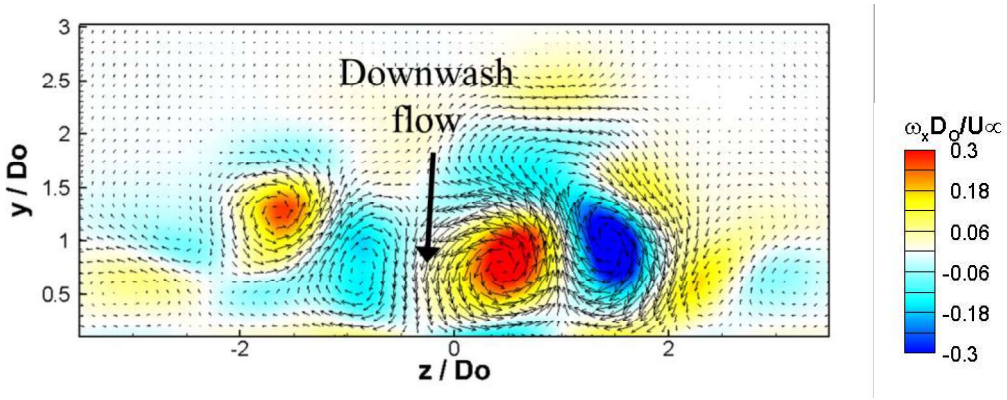

Contour of time-averaged streamwise vorticity with velocity vectors obtained from CFD simulation in the attached boundary layer in spanwise plane at $x = 18D_o$ at phase difference $\Delta\phi = \pi/2$ and yaw angle $\psi = \pi/4$.

Figure 8

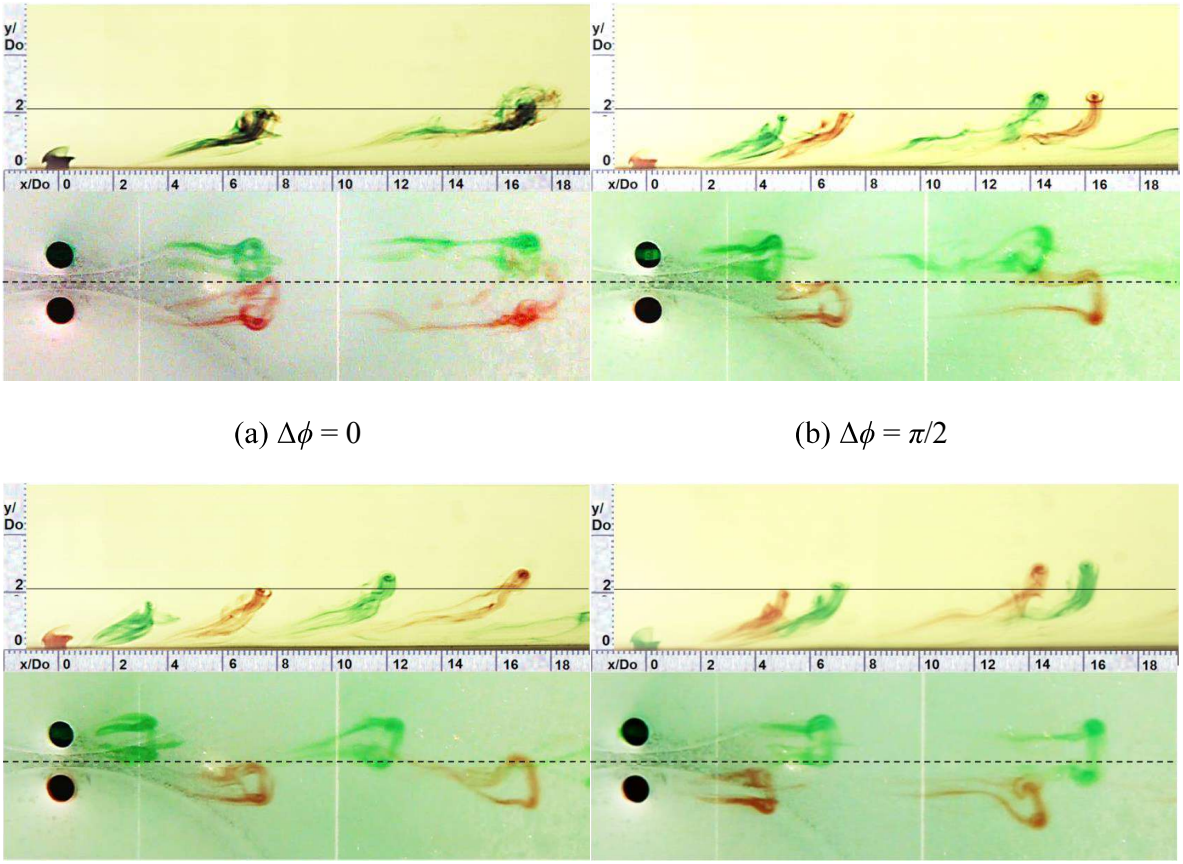

(a) $\Delta\phi = 0$ (b) $\Delta\phi = \pi/2$

(c) $\Delta\phi = \pi$ (d) $\Delta\phi = 3\pi/2$

Stereoscopic dye visualizations of twin SJs at yaw angle $\psi = \pi/2$ with four phase differences $\Delta\phi$.

Figure 9

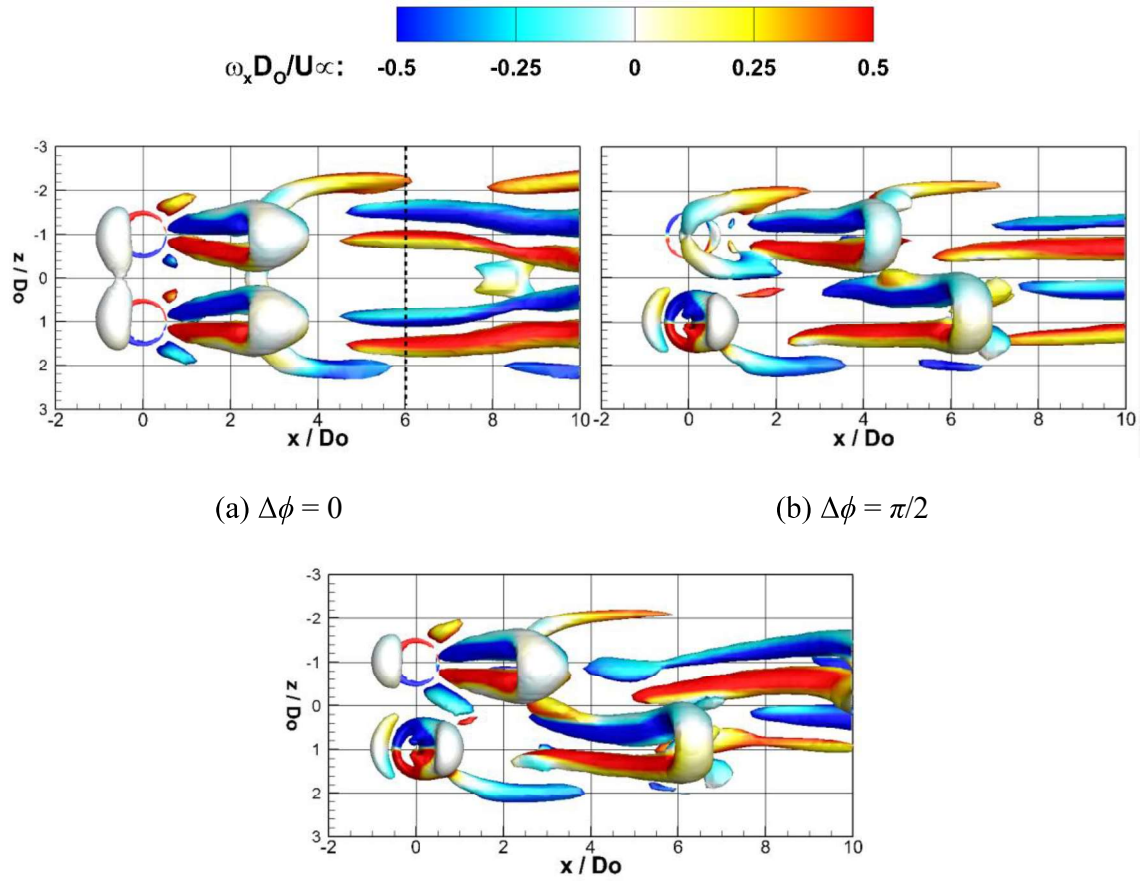

(a) $\Delta\phi = 0$ (b) $\Delta\phi = \pi/2$

(c) $\Delta\phi = \pi$

Bottom views of instantaneous flow structures plotted with $Q = 30$ from CFD simulations at yaw angle $\psi = \pi/2$ with three phase differences $\Delta\phi$. The dash line in Fig. 9(a) indicates the selected spanwise-wall-normal plane in Fig. 10.

Figure 10

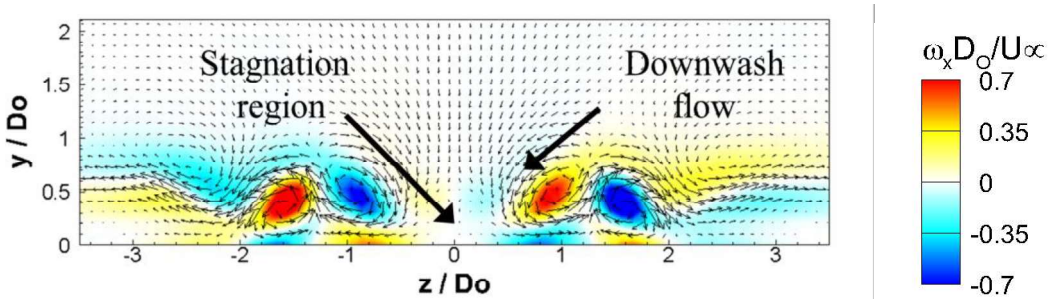

Contour of streamwise vorticity with velocity vectors in a spanwise-wall-normal plane at $x = 6D_o$ in the case of twin SJs at phase difference $\Delta\phi = 0$ and yaw angle $\psi = \pi/2$ at the phase of maximum ingestion of the SJ actuators.

Figure 11

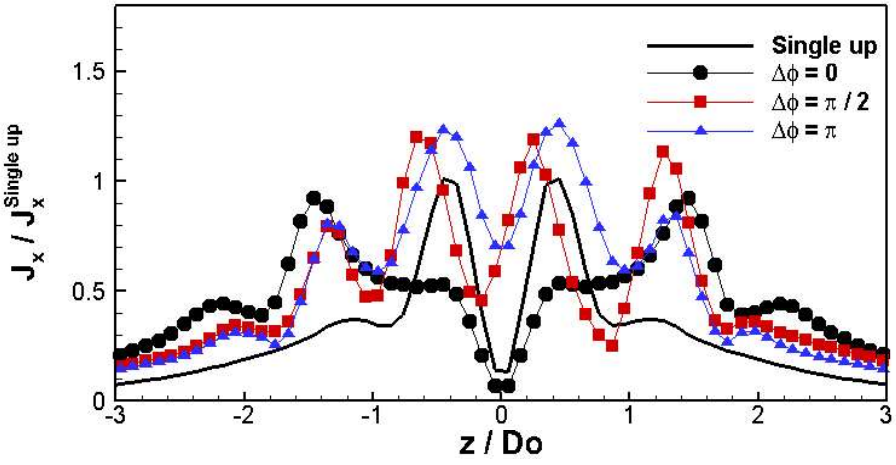

Spanwise distribution of time-averaged streamwise vorticity flux in a wall-normal plane at $x = 6D_o$ in single SJ case and twin SJ cases at yaw angle $\psi = \pi/2$ with three phase differences $\Delta\phi$.

Figure 12

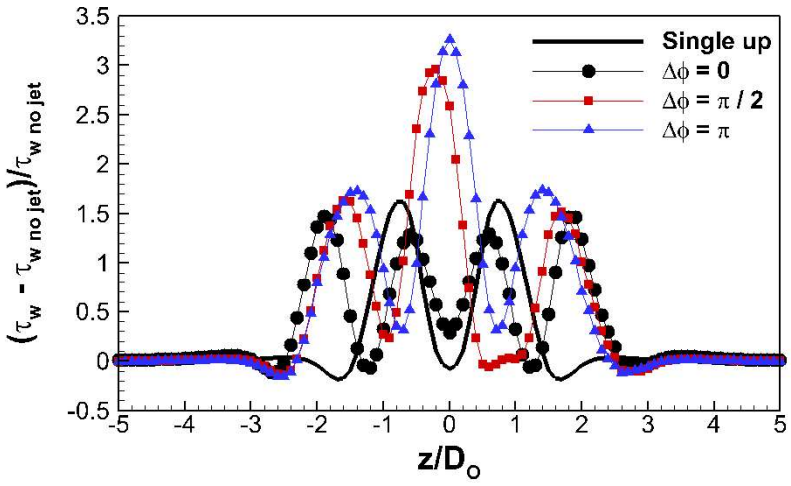

(a)

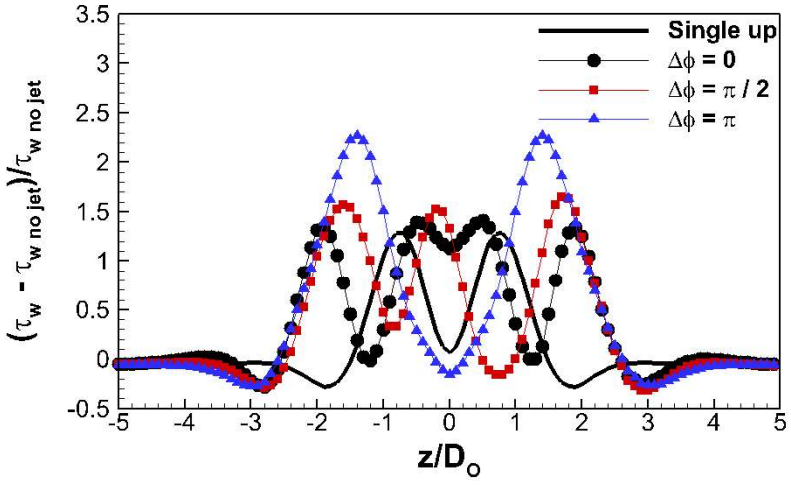

(b)

Spanwise distribution of time-averaged excess wall shear stress at (a) $x = 6D_o$ and (b) $x = 18D_o$ at yaw angle $\psi = \pi/2$ with three phase differences $\Delta\phi$.

Figure 13

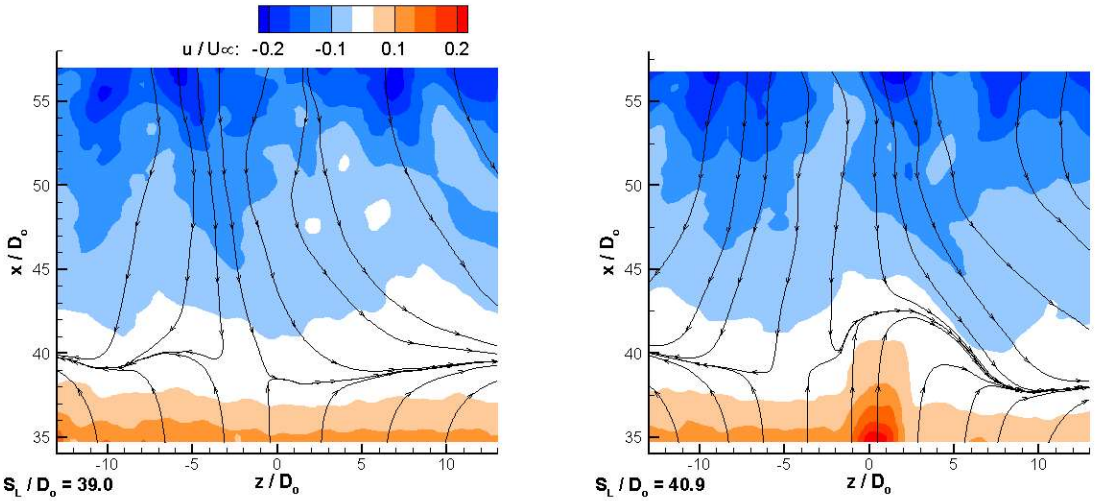

(a) Baseline case (b) Single SJs

Contour of time-averaged streamwise velocity with streamlines from PIV measurement in the plane parallel to the inclined plate in (a) uncontrolled case, (b) single SJ case.

Figure 14

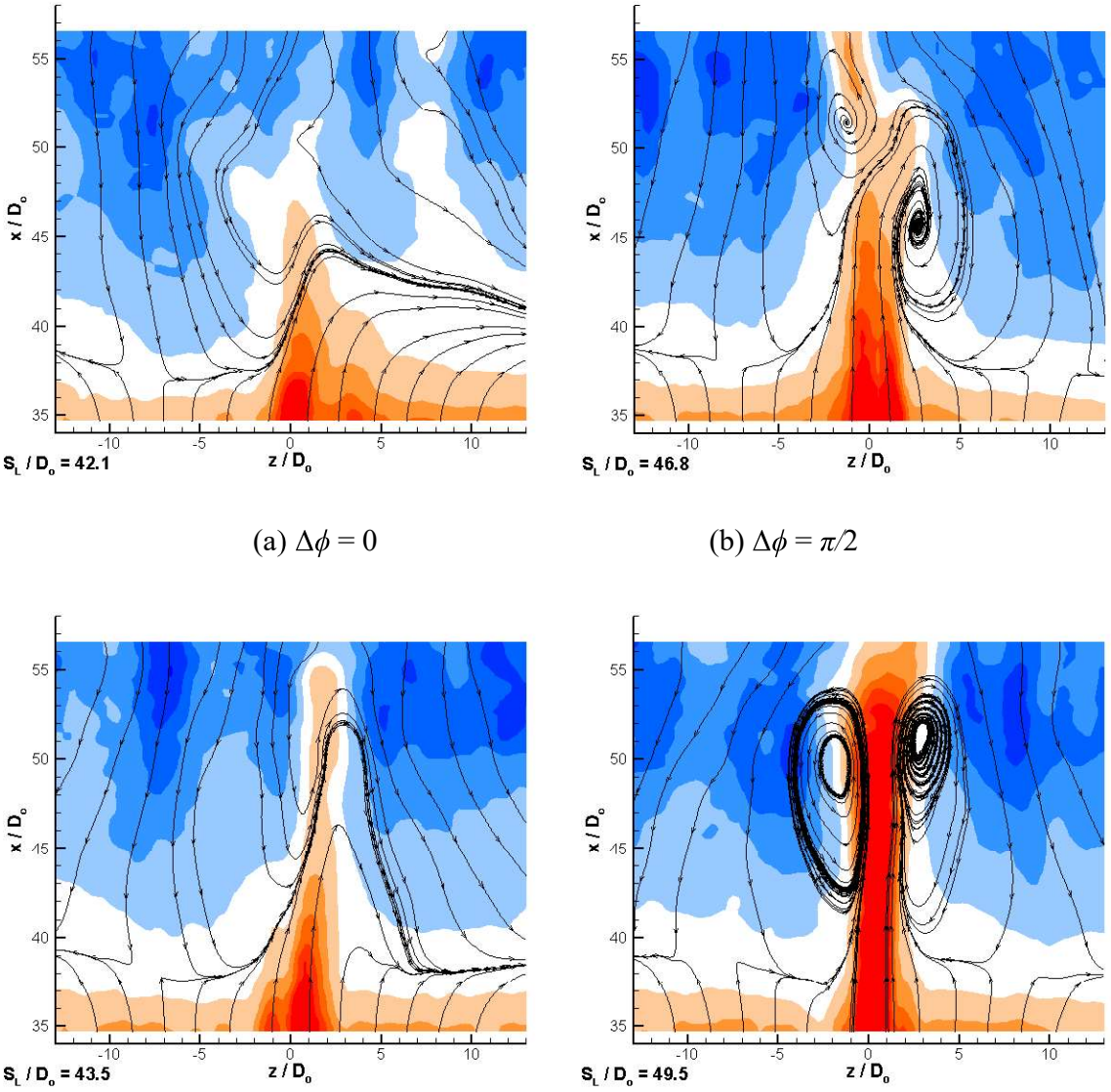

(a) $\Delta\phi = 0$ (b) $\Delta\phi = \pi/2$

(c) $\Delta\phi = \pi$ (d) $\Delta\phi = 3\pi/2$

Contour of time-averaged streamwise velocity with streamlines from PIV measurement in the plane parallel to the inclined plate in twin SJs cases at yaw angle $\psi = \pi/4$ with four phase differences $\Delta\phi$.

Figure 15

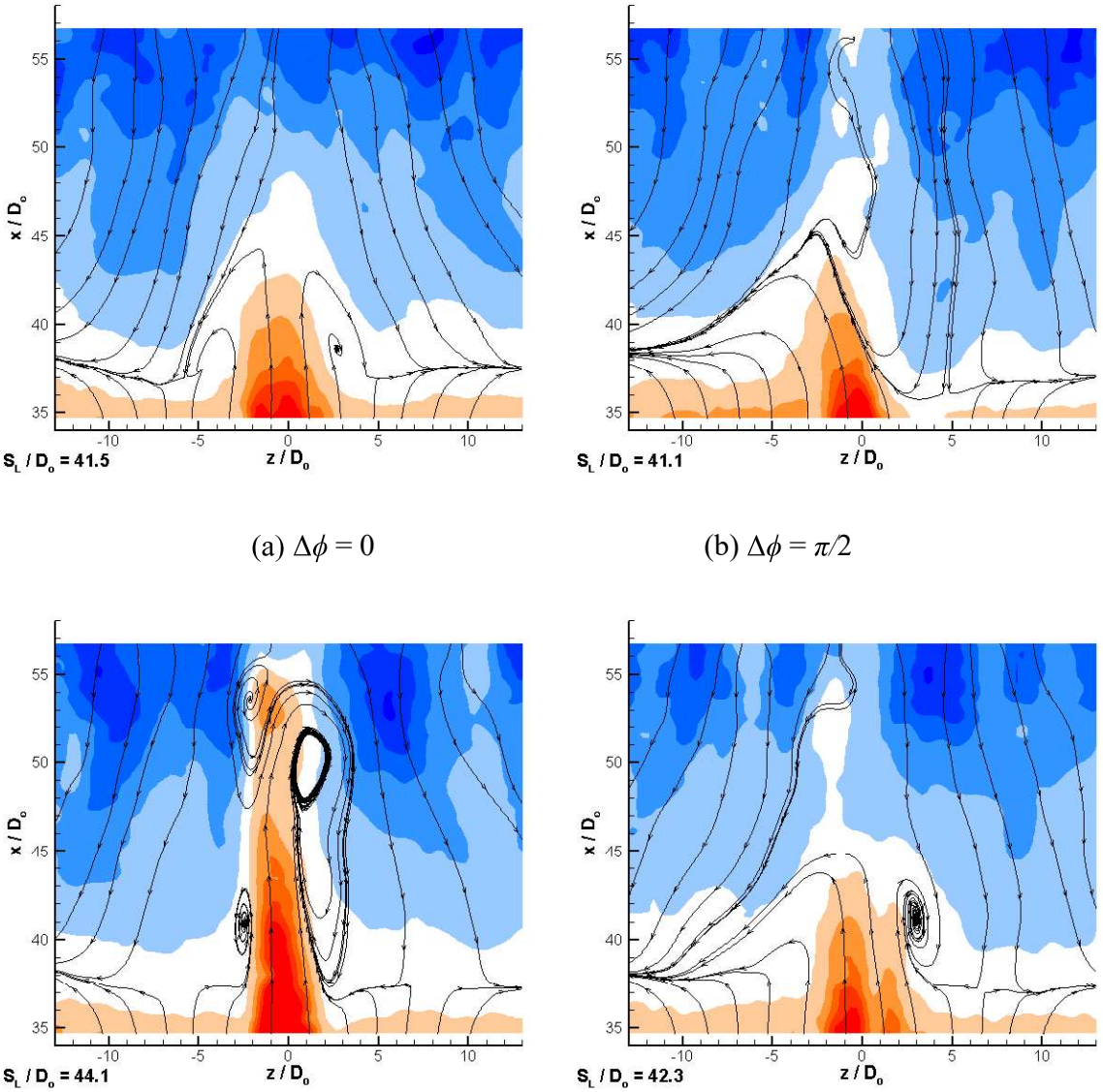

(a) $\Delta\phi = 0$ (b) $\Delta\phi = \pi/2$

(c) $\Delta\phi = \pi$ (d) $\Delta\phi = 3\pi/2$

Contour of time-averaged streamwise velocity with streamlines from PIV measurement in the plane parallel to the inclined plate in twin SJ cases at yaw angle $\psi = \pi/2$ with four phase differences $\Delta\phi$.